

Uncalibrated photometric stereo refined by polarization angle

Daisuke Miyazaki · Shuhei Hashimoto

Received: date / Accepted: date

Abstract Photometric stereo allows us to estimate the surface normal of an object based on its shading. In uncalibrated photometric stereo, the light source direction is unknown; thus, both the light source direction and surface normal should be estimated, which establishes an ill-posed problem with ambiguity in its solution. Consequently, assumptions should be made to uniquely determine the solution; however, assumptions are not always satisfied in practice, which results in an estimated surface normal that differs from the true surface normal. To improve surface normal estimation, we analyze the polarization state of reflected light considering that polarization can constrain the possible orientation of the surface normal. Thereafter, through extensive experimental evaluations, we demonstrate that polarization effectively improves uncalibrated photometric stereo.

Keywords Polarization · Shape-from-X · Surface normal · Photometric stereo · Uncalibrated photometric stereo

1 Introduction

Uncalibrated photometric stereo in which light source directions are unknown lacks a unique solution when determining the surface normal of an object. Although assumptions can be made for disambiguation, they may not be satisfied

Daisuke Miyazaki
Hiroshima City University
3-4-1 Ozukahigashi Asaminami-ku, Hiroshima, Japan
E-mail: miyazaki@hiroshima-cu.ac.jp

Shuhei Hashimoto
Hiroshima City University
3-4-1 Ozukahigashi Asaminami-ku, Hiroshima, Japan
E-mail: shuhei@ime.info.hiroshima-cu.ac.jp
Present Address: Mitsubishi Electric Control Software Corporation, Kobe, Japan

in practice. In this study, we analyze the polarization state of reflected light to improve surface normal estimation accuracy in uncalibrated photometric stereo.

Shading comprises albedo (i.e., diffuse reflectance), a surface normal, and a light source direction, which are unknown in uncalibrated photometric stereo. To uniquely determine the surface normal of an object, we constrain light and the normal itself. These constraints may not be satisfied in practice; thus, we also consider the polarization state of reflected light, which depends on the surface normal, to further refine the estimation.

2 Related work

Photometric stereo [1] with unknown light source direction is referred to as uncalibrated photometric stereo [2–15].

Hayakawa [3] proved that uncalibrated photometric stereo can be solved if the light source brightness (i.e., object albedo) is uniform, and this was confirmed in Corollary 4.1 by Belhumeur et al. [6]. Similarly, we assume the light source brightness to be uniform. In addition, Hayakawa [3] and Belhumeur et al. [6] proved that three or more normal values should be known to obtain the solution. Accordingly, we use the known surface normal of the occluding boundary.

Wolff and Boult [16] developed a basic theory to demonstrate that shape from polarization can constrain the surface normal. Then, Rahmann and Canterakis [17] applied this constraint to estimate the surface normal of a specular object from multiple views. Atkinson and Hancock [18] analyzed the local structure of an object between two viewpoints to calculate the surface normal from the polarization of two views. In addition, Atkinson and Hancock [19] thoroughly investigated the surface normal estimation of a diffuse object from a single view. In addition to the surface normal, Huynh et al. [20] estimated the refractive index. In these studies, polarization facilitated the estimation of the surface normal. Similarly, we leverage polarization to constrain the surface normal to improve the accuracy of uncalibrated photometric stereo.

Atkinson and Hancock [21] used photometric information to uniquely determine the surface normal because there is ambiguity when uniquely determining the surface normal via polarization. Using both photometric information and polarization information is also useful for uncalibrated photometric stereo. For example, Drbohlav and Sara [22] used polarization for uncalibrated photometric stereo and proved that the polarizer should be set in front of the light source to uniquely determine the surface normal of the object. In addition, Ngo et al. [23] obtained the surface normal without restricting the polarizer position. However, they made assumptions, and the refractive index should be estimated to calculate the surface normal. In contrast, the proposed method does not require refractive index estimation. In addition, to the best of our knowledge, no mathematical proof for the solution has been provided for the iterative computations in those methods [22, 23], whereas the proposed method

is based on linear algebra, and the unique solution is explained mathematically. The two similar methods [22,23] indicate that polarization provides a strong cue for uncalibrated photometric stereo but is imperfect; therefore, the proposed method relies on a robust method commonly employed in uncalibrated photometric stereo that does not employ polarization. We then employ polarization to further refine the surface normal estimate. The proposed method for polarization-based uncalibrated photometric stereo uniquely determines the surface normal with robustness, stability, and reliability. In addition, the correctness of the proposed method is proven mathematically.

3 Uncalibrated photometric stereo

3.1 Lambert reflection

Consider an object obeying the Lambertian reflection model and a far point light source. Observed brightness i can be represented as follows:

$$i = \mathbf{s} \cdot \mathbf{l}, \quad (1)$$

or $\mathbf{s} = (s_x, s_y, s_z)^\top$ is the surface vector and unit vector $\mathbf{l} = (l_x, l_y, l_z)^\top$ is the light source vector. Surface vector \mathbf{s} is a product of the albedo and normal vector, and light source vector \mathbf{l} represents the light direction.

As $\mathbf{s} \cdot \mathbf{l}$ may become negative, Eq. (1) is typically formulated as $i = \max(\mathbf{s} \cdot \mathbf{l}, 0)$. However, photometric linearization [24–30] forces the images to obey Eq. (1). Thus, in the proposed method, we apply photometric linearization to the input images.

The $P \times 3$ surface matrix \mathbf{S} is a concatenation of surface vectors and the $3 \times F$ light matrix \mathbf{L} , which is a concatenation of light vectors, where P is the number of pixels in an image, and F is the number of images:

$$\mathbf{S} = \begin{pmatrix} s_{1x} & s_{1y} & s_{1z} \\ s_{2x} & s_{2y} & s_{2z} \\ \vdots & \vdots & \vdots \\ s_{Px} & s_{Py} & s_{Pz} \end{pmatrix}, \quad (2)$$

$$\mathbf{L} = \begin{pmatrix} l_{x1} & l_{x2} & \dots & l_{xF} \\ l_{y1} & l_{y2} & \dots & l_{yF} \\ l_{z1} & l_{z2} & \dots & l_{zF} \end{pmatrix}. \quad (3)$$

The input data are represented by matrix \mathbf{I} :

$$\mathbf{I} = \mathbf{S}\mathbf{L} = \begin{pmatrix} i_{11} & i_{12} & \dots & i_{1F} \\ i_{21} & i_{22} & \dots & i_{2F} \\ \vdots & \vdots & \ddots & \vdots \\ i_{P1} & i_{P2} & \dots & i_{PF} \end{pmatrix}. \quad (4)$$

As the rank of both the surface matrix \mathbf{S} and light matrix \mathbf{L} is 3, Eq. (4) implies that the rank of matrix \mathbf{I} is also 3.

3.2 Singular value decomposition

We apply photometric linearization [24–30] to input image i to obtain shading image \hat{i} . Here, the pixel brightness of the p -th pixel from image f is denoted \hat{i}_{pf} .

Image matrix $\hat{\mathbf{I}}$ locates the pixels of the shading image vertically and the images horizontally as follows:

$$\hat{\mathbf{I}} = \begin{pmatrix} \hat{i}_{11} & \hat{i}_{12} & \cdots & \hat{i}_{1F} \\ \hat{i}_{21} & \hat{i}_{22} & \cdots & \hat{i}_{2F} \\ \vdots & \vdots & \ddots & \vdots \\ \hat{i}_{P1} & \hat{i}_{P2} & \cdots & \hat{i}_{PF} \end{pmatrix}. \quad (5)$$

We apply singular value decomposition (SVD) to the image matrix:

$$\hat{\mathbf{I}} = \mathbf{U}\mathbf{W}\mathbf{V}^\top. \quad (6)$$

Here, the rank of image matrix $\hat{\mathbf{I}}$ is 3. By extracting three components from the $P \times F$ left singular matrix \mathbf{U} , $F \times F$ singular value matrix \mathbf{W} , and $F \times F$ right singular matrix \mathbf{V}^\top , we obtain matrices \mathbf{U}' , \mathbf{W}' , and \mathbf{V}'^\top with dimensions $P \times 3$, 3×3 , and $3 \times F$, respectively. Thus, we obtain:

$$\mathbf{I}' = \mathbf{U}'\mathbf{W}'\mathbf{V}'^\top. \quad (7)$$

Pseudo-surface matrix \mathbf{S}' and pseudo-light matrix \mathbf{L}' are given as follows.

$$\mathbf{S}' = \mathbf{U}'\mathbf{W}', \quad \mathbf{L}' = \mathbf{V}'^\top. \quad (8)$$

However, these matrices are not the true surface and light matrices. In fact, the ambiguity between \mathbf{S}' and \mathbf{L}' represented by matrix \mathbf{A} should be solved to uniquely determine true surface matrix \mathbf{S} and true light matrix \mathbf{L} . Ambiguity matrix \mathbf{A} is a 3×3 regular matrix satisfies [2–4, 6]:

$$\mathbf{S} = \mathbf{S}'\mathbf{A}^{-1}, \quad \mathbf{L} = \mathbf{A}\mathbf{L}'. \quad (9)$$

3.3 Constant brightness constraint

We use the same light source to capture input images; therefore, we can solve ambiguity matrix \mathbf{A} by constraining the light source brightness to be constant [3].

True light vector \mathbf{l}_f can be obtained by multiplying pseudo-light vector \mathbf{I}'_f by ambiguity matrix $\tilde{\mathbf{A}}$:

$$\mathbf{l}_f = \tilde{\mathbf{A}}\mathbf{I}'_f. \quad (10)$$

The norm of the light vector represents the squared brightness, i.e., $\mathbf{l}_f^\top \mathbf{l}_f$ or $\mathbf{l}'_f{}^\top \tilde{\mathbf{A}}^\top \tilde{\mathbf{A}} \mathbf{l}'_f$. We define symmetrical matrix \mathbf{B} as follows:

$$\mathbf{B} = \tilde{\mathbf{A}}^\top \tilde{\mathbf{A}} = \begin{pmatrix} b_1 & b_4 & b_6 \\ b_4 & b_2 & b_5 \\ b_6 & b_5 & b_3 \end{pmatrix}. \quad (11)$$

The constraint that forces the squared brightness to be one is expressed as follows:

$$\mathbf{l}'_f{}^\top \mathbf{B} \mathbf{l}'_f = 1. \quad (12)$$

Equation (12) can be rewritten as follows:

$$\begin{pmatrix} l'_{xf}{}^2 & l'_{yf}{}^2 & l'_{zf}{}^2 & 2l'_{xf}l'_{yf} & 2l'_{yf}l'_{zf} & 2l'_{zf}l'_{xf} \end{pmatrix} \cdot \begin{pmatrix} b_1 & b_2 & b_3 & b_4 & b_5 & b_6 \end{pmatrix}^\top = 1. \quad (13)$$

We concatenate Eq. (13) for F images to obtain the following expressions:

$$\begin{aligned} \mathbf{C} \mathbf{b} &= \mathbf{1}, \\ \mathbf{C} &= \begin{pmatrix} l'_{x1}{}^2 & l'_{y1}{}^2 & \cdots & 2l'_{z1}l'_{x1} \\ l'_{x2}{}^2 & l'_{y2}{}^2 & \cdots & 2l'_{z2}l'_{x2} \\ \vdots & \vdots & \ddots & \vdots \\ l'_{xF}{}^2 & l'_{yF}{}^2 & \cdots & 2l'_{zF}l'_{xF} \end{pmatrix}, \\ \mathbf{b} &= (b_1 \ b_2 \ \dots \ b_6)^\top, \\ \mathbf{1} &= (1 \ 1 \ \dots \ 1)^\top, \end{aligned} \quad (14)$$

whose solution provides \mathbf{b} :

$$\mathbf{b} = \mathbf{C}^+ \mathbf{1}. \quad (15)$$

Symmetrical matrix \mathbf{B} can be rearranged by Eq. (11) from \mathbf{b} . As \mathbf{B} is symmetrical, its SVD is given as follows:

$$\mathbf{B} = \mathbf{U}_B \mathbf{W}_B \mathbf{U}_B^\top. \quad (16)$$

Hence, ambiguity matrix $\tilde{\mathbf{A}}$ can be calculated from \mathbf{B} as follows:

$$\tilde{\mathbf{A}} = \mathbf{W}_B^{1/2} \mathbf{U}_B^\top. \quad (17)$$

We update pseudo-surface matrix \mathbf{S}' and pseudo-light matrix \mathbf{L}' using the obtained ambiguity matrix $\tilde{\mathbf{A}}$ as follows:

$$\mathbf{S}'' = \mathbf{S}' \tilde{\mathbf{A}}^{-1}, \quad \mathbf{L}'' = \tilde{\mathbf{A}} \mathbf{L}'. \quad (18)$$

Finally, we represent the remaining ambiguity as orthogonal matrix \mathbf{R} satisfying:

$$\mathbf{S} = \mathbf{S}'' \mathbf{R}, \quad \mathbf{L} = \mathbf{R}^\top \mathbf{L}'', \quad (19)$$

which is solved in Sect. 4.2.

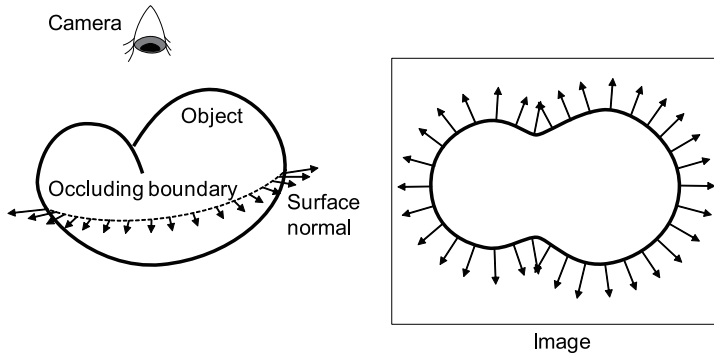


Fig. 1 Occluding boundary in a captured image

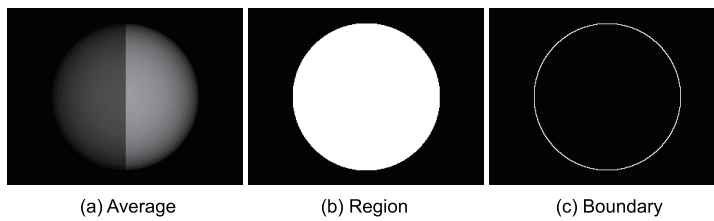


Fig. 2 Computation of occluding boundary: **a** average image, **b** object (white) and background (black) regions, and **c** occluding boundary

4 Occluding boundary

4.1 Surface normal at occluding boundary

The occluding boundary of an object contour is that observed in a captured image, as shown in Fig. 1.

We should detect the boundary of the object from the image. Here, we calculate the average image (Fig. 2a) from multiple input images. Thresholding the brightness of the average image provides the object region, which is shown in white in Fig. 2b, where the black region represents the background. The boundary between the white and black regions is the occluding boundary (Fig. 2c).

After detecting the occluding boundary, we calculate its surface normal under the assumption that the object is geometrically smooth and closed. We consider the direction from the object to the camera to be the z -axis. Differential geometry proves that the surface normal to the occluding boundary is parallel to the xy plane and points outward from the object to the background region.

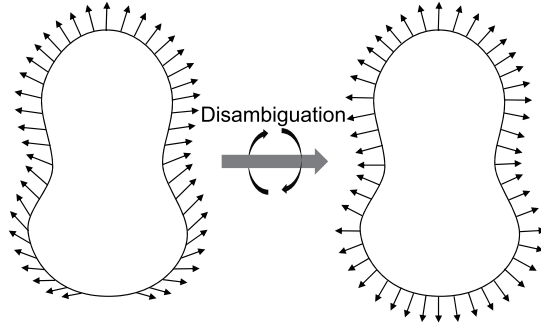


Fig. 3 Occluding boundary constraint

4.2 Occluding boundary constraint

As mentioned in Sect. 3.3, we constrain the length of \mathbf{l} and obtain pseudo-surface matrix \mathbf{S}'' . However, an ambiguity preserving the length but deforming the other components remains. As a result, the pseudo-surface normal calculated from the SVD is distorted (Fig. 3). Here, we use the surface normal at the occluding boundary (Sect. 4.1) to estimate ambiguity matrix \mathbf{A} [30].

The updated ambiguity matrix \mathbf{A}' is obtained by solving the following equation:

$$\mathbf{S}''' = \mathbf{S}'' \mathbf{A}'. \quad (20)$$

The pixels at the occluding boundary (Sec. 4.1) are used for \mathbf{S}''' . For occluding boundary matrix \mathbf{S}''' and pseudo-surface matrix \mathbf{S}'' , we concatenate \tilde{P} pixels from the occluding boundary pixels. Theoretically, the surface normal (n'_x, n'_y, n'_z) at the occluding boundary obeys $n'_z = 0$ because it belongs to the xy plane; thus, the rank of the matrix is 2 rather than 3 if we concatenate these vectors. Therefore, we embed $n'_z = c_z$, where c_z is a small positive constant, to increase the rank to 3, and the row of the occluding boundary matrix is represented as $(s'''_{x\tilde{P}}, s'''_{y\tilde{P}}, s'''_{z\tilde{P}}) = (n'_x, n'_y, c_z)$.

$$\begin{pmatrix} s'''_{x1} & s'''_{y1} & s'''_{z1} \\ s'''_{x2} & s'''_{y2} & s'''_{z2} \\ \vdots & \vdots & \vdots \\ s'''_{x\tilde{P}} & s'''_{y\tilde{P}} & s'''_{z\tilde{P}} \end{pmatrix} = \begin{pmatrix} s''_{x1} & s''_{y1} & s''_{z1} \\ s''_{x2} & s''_{y2} & s''_{z2} \\ \vdots & \vdots & \vdots \\ s''_{x\tilde{P}} & s''_{y\tilde{P}} & s''_{z\tilde{P}} \end{pmatrix} \begin{pmatrix} a'_{00} & a'_{01} & a'_{02} \\ a'_{10} & a'_{11} & a'_{12} \\ a'_{20} & a'_{21} & a'_{22} \end{pmatrix}. \quad (21)$$

By multiplying pseudo-inverse \mathbf{S}''^{+} from the left to Eq. (21), we obtain:

$$\mathbf{A}' = \mathbf{S}''^{+} \mathbf{S}'''. \quad (22)$$

Thus, ambiguity matrix \mathbf{A}' is obtained; however, matrix \mathbf{A}' does not strictly satisfy orthogonality due to errors. To make ambiguity matrix \mathbf{A}' orthogonal, we use its SVD:

$$\mathbf{A}' = \mathbf{U}_R \mathbf{W}_R \mathbf{V}_R^T. \quad (23)$$

If we force matrix \mathbf{W}_R to be the identity matrix, the ambiguity matrix becomes an orthogonal matrix \mathbf{R} :

$$\mathbf{R} = \mathbf{U}_R \mathbf{V}_R^\top, \quad (24)$$

which can improve the pseudo-surface matrix \mathbf{S}'' . Finally, the updated surface matrix, \mathbf{S} , is obtained as follows:

$$\mathbf{S} = \mathbf{S}'' \mathbf{R}. \quad (25)$$

5 Shape from polarization

5.1 Polarization

The proposed uncalibrated photometric stereo based on existing approaches (Sects. 3 and 4) uniquely and robustly determines the surface normal of an object using a mathematical derivation. However, these constraints may not always work; thus, we refine the surface normal using polarization information.

Light is an electromagnetic wave, and when light oscillates in one direction, it is said to be a perfect linear polarization. In contrast, unpolarized light oscillates in all directions. Here, we use unpolarized light to illuminate the object and observe the diffusely reflected light passing through a polarizer. The maximum and minimum light brightness values observed while rotating the polarizer are denoted I_{\max} and I_{\min} , respectively. Then, the surface normal is represented in polar coordinates with the azimuth and zenith angles denoted ϕ and θ , respectively. The orientation from the surface point to the camera corresponds to the z -axis, and the plane containing the reflected light and surface normal vectors is referred to as the reflection plane. The orientation of the reflection plane is the same as azimuth angle ϕ or $\phi + 180^\circ$, which is defined in the image coordinates.

If the polarizer angle coincides with the reflection plane, the minimum brightness value I_{\min} is observed in specular reflection, and the maximum brightness value I_{\max} is observed in diffuse reflection. Here, we assume that the image pixels are diffuse-dominant, i.e., all pixels cause diffuse reflection. Therefore, the polarizer angle at brightness value I_{\max} coincides with ϕ and $\phi + 180^\circ$. Note that the azimuth angle calculated from polarization has an 180° ambiguity because the cycle of the linear polarizer is 180° , and the azimuth angle of the surface normal is either ϕ or $\phi + 180^\circ$.

Figure 4 illustrates the polarization constraint. In the camera coordinate system, the z -axis is along the optical axis. The reflection plane angle ϕ is the angle between the x -axis of the camera coordinate system and the intersecting line between the reflection and xy planes. As shown in Fig. 4, the surface normal is included in the reflection plane; therefore, despite the abovementioned ambiguity, the azimuth angle obtained from polarization analysis can constrain the surface normal.

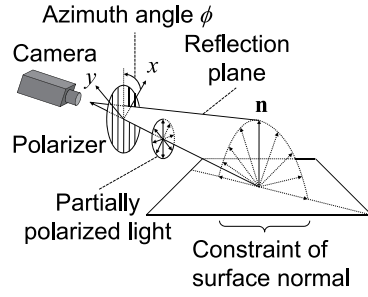


Fig. 4 Relationship between surface normal and reflection plane when observed from a single viewpoint

5.2 Azimuth angle calculation

A polarization camera can be used to measure the azimuth angle. Here, we use multiple input polarization images captured under different light directions and aggregate the azimuth images into a single image.

As the average angle cannot be calculated directly due to periodicity (i.e., 0 and 360° correspond to the same point), we represent each angle as a vector and calculate the average across vectors. Then, the angle is retrieved from the average vector as follows:

$$\phi_x = \cos(2\nu), \phi_y = \sin(2\nu). \quad (26)$$

As the range of the polarizer angle is $0 \leq \nu < \pi$; thus, we double the angle to map the range onto $0 \leq \nu < 2\pi$. The average values of ϕ_x and ϕ_y are denoted $\bar{\phi}_x$ and $\bar{\phi}_y$, respectively, and F is number of images. For example, averaging 1 and $2\pi - 1$ will be π , but averaging 1 (rad) and $2\pi - 1$ (rad) should be 0 (rad). To solve this problem, it is necessary to consider the angle in vector space. In other words, the average of $(\cos 1, \sin 1)$ and $(\cos(2\pi - 1), \sin(2\pi - 1))$ is $(1, 0)$. The average vectors are calculated as follows:

$$\bar{\phi}_x = \frac{\sum_{i=1}^F \phi_{xi}}{F}, \bar{\phi}_y = \frac{\sum_{i=1}^F \phi_{yi}}{F}. \quad (27)$$

Azimuth angle ϕ can be calculated from $\bar{\phi}_x$ and $\bar{\phi}_y$ as follows:

$$\phi = \frac{1}{2} \arctan \left(\frac{\bar{\phi}_y}{\bar{\phi}_x} \right). \quad (28)$$

Since we double ν , we divide the arctangent with 2, as shown in Eq. (28). As a result, azimuth angle ϕ is obtained in the range from 0 (rad) to π (rad). This angle, ranges from 0 (rad) to π (rad), is not unique in the range 0 (rad) to 2π (rad); however, this ambiguity is solved using the surface normal obtained in Sect. 4.2.

The azimuth angle calculation is illustrated in Fig. 5.

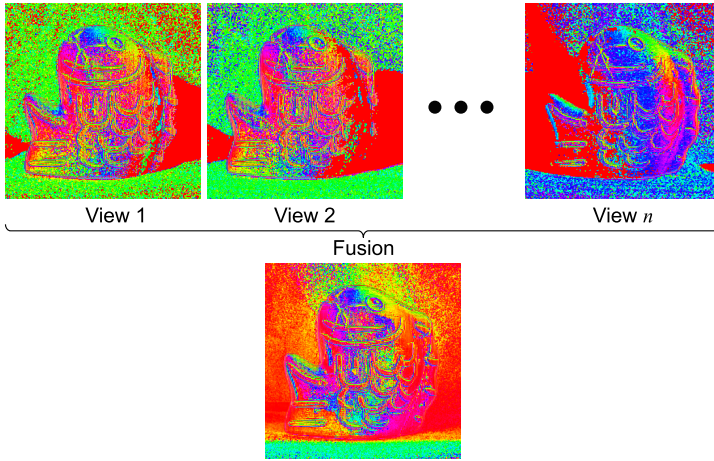


Fig. 5 Example of azimuth angle calculation

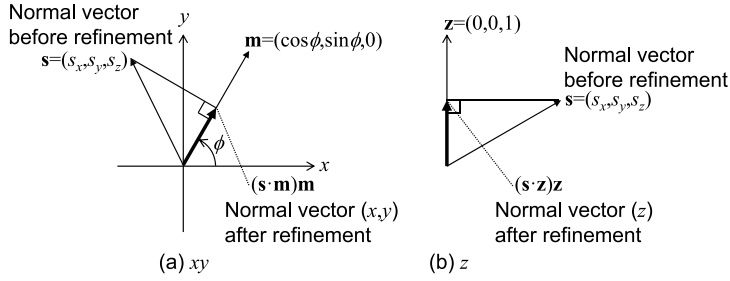


Fig. 6 Refinement of surface normal: **a** polarization constraints and **b** preservation of z -axis component

5.3 Polarization-based refinement

Although the surface normal described by Eq. (25) is adequate in most cases, it can be improved using the azimuth angle derived in Sect. 5.2 (Fig. 6a).

Vector $\mathbf{m} = (\cos \phi, \sin \phi, 0)$ in Fig. 6a represents the azimuth angle ϕ described by Eq. (28). Here, the surface normal \mathbf{s} (Sect. 4.2) is normalized as $\hat{\mathbf{s}}$. Then, surface normal $\hat{\mathbf{s}}$ can be corrected for its orientation to coincide with that of \mathbf{m} as follows:

$$\mathbf{n}_{xy} = (\hat{\mathbf{s}} \cdot \mathbf{m})\mathbf{m}. \quad (29)$$

Equation (29) only considers the x - and y -axis components; thus, we calculate the z -axis component, as shown in Fig. 6b. The following equation forces surface normal \mathbf{s} to have the same direction as the z axis, i.e., $\mathbf{z} = (0, 0, 1)$, to obtain the z -axis component of the vector as follows:

$$\mathbf{n}_z = (\hat{\mathbf{s}} \cdot \mathbf{z})\mathbf{z}. \quad (30)$$

By adding Eq. (29) and Eq. (30), we obtain the following 3D surface normal vector:

$$\tilde{\mathbf{n}} = \mathbf{n}_{xy} + \mathbf{n}_z. \quad (31)$$

We normalize $\tilde{\mathbf{n}}$ to obtain vector $\hat{\mathbf{n}}$. Although the azimuth angle is calculated using Eq. (28), if the surface normal points to the camera direction, i.e., $(0, 0, 1)$, the angle becomes unreliable. Mathematically, the azimuth angle is undetermined if the zenith angle is 0. Therefore, we weight this constraint (Eq. (31)) according to whether the surface normal points to the camera. Specifically, we apply a high weight if the surface normal points perpendicularly to the camera and a low weight if the surface normal points to the camera.

$$\mathbf{n} = (\hat{\mathbf{s}} \cdot \mathbf{z})\hat{\mathbf{s}} + \{1 - (\hat{\mathbf{s}} \cdot \mathbf{z})\}\hat{\mathbf{n}}. \quad (32)$$

The final result is the normal vector calculated by normalizing \mathbf{n} in Eq. (32).

5.4 Algorithm

The constraints used in the proposed method are convincing. The constant brightness constraint (Sect. 3.3) and occluding boundary constraint (Sect. 4.2) are proved to be mathematically convincing to solve the ambiguity of surface normal. The most important point of this method is the constraint using polarization (Sect. 5.3). In addition, the balance between the photometric and polarimetric constraints is important. The proposed method adequately weights each constraint. For 0° , there is no shadow; thus, we apply a heavier weight to the photometric constraint. In contrast, for 90° , the degree of polarization is the maximum; thus, we apply a heavier weight to the polarization constraint.

Some existing techniques use the zenith angle of the surface normal as a cue [18–21] because it can be calculated from the degree of polarization. The correspondence between the degree of polarization and zenith angle is one-to-one for diffuse reflection. However, the degree of polarization depends on the index of refraction (IOR) (Fig. 7a) and the surface roughness [31] (Fig. 7b). The unknown parameters (i.e., the IOR and surface roughness) would increase; thus, we did not constrain the zenith angle with the degree of polarization.

However, we agree that constraining the zenith angle using the degree of polarization is useful; therefore, constraining the zenith angle using the degree of polarization may improve the proposed method.

6 Experimental results

6.1 Experimental equipment

The experimental environment used to capture images in this study is shown in Fig. 8a. We fixed the camera and target object, and we captured images

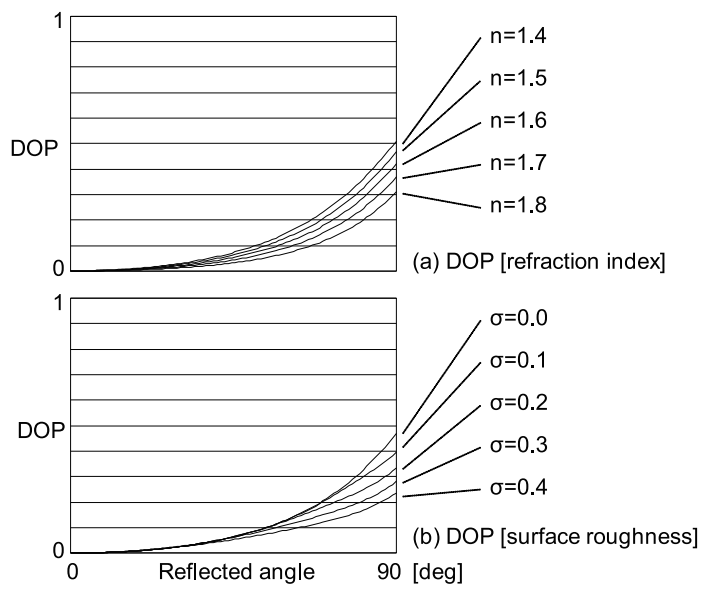


Fig. 7 Degree of polarization: **a** surface roughness is zero, and the index of refraction (IOR) is 1.4, 1.5, ..., 1.8, and **b** IOR is 1.7, and the surface roughness is 0, 0.1, ..., 0.4

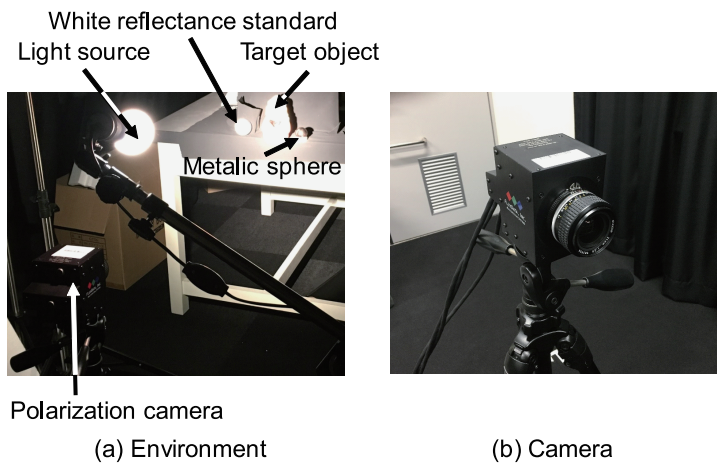


Fig. 8 Experimental setup: **a** environment for capturing images and **b** camera used in this study

Table 1 Camera specifications

| | |
|------------------|---|
| Manufacturer | FluxData, Inc. |
| Model | FD1665P |
| Sensor | Sony ICX414 x3 1/2CCD (charge-coupled device) color |
| Resolution | 659 × 494 |
| Pixel size | 9.9 μ m × 9.9 μ m |
| Configuration | Polarization 3 channel (0, 45, and 90°) |
| Frame rate | 74fps (output tone depends on pixel format) |
| Output interface | 1394/b |
| Software | Capture software and development toolkit |
| Lens | Nikon 24mm f/2.8 |
| Internal camera | Scout OEM (original equipment manufacturer) on-board camera ×3 (BASLER AG) |

Table 2 Surface normal error of virtual sphere as corresponding constraint is added to estimation

| | SVD | Constant brightness | Occluding boundary | Polarization |
|---------------------|-------|------------------------|-----------------------|--------------|
| Average error (rad) | 1.555 | 2.764 | 0.000 | 0.000 |
| Minimum error (rad) | 0.938 | 2.696 | 0.000 | 0.000 |
| Maximum error (rad) | 2.956 | 3.079 | 0.000 | 0.000 |

under different light directions. In addition, the white reflectance standard was used to calibrate the polarization camera.

A photograph of the polarization camera is shown in Fig. 8b, and its specifications are listed in Table 1.

6.2 Virtual sphere

First, we conducted a simulation using 30 input polarization images of a virtual sphere. Figures 9a–d show the target object, its occluding boundary, its azimuth angle, and the surface normal, respectively. The azimuth angle with 180° ambiguity shown in Fig. 9c is color coded, where the hue represents the orientation. The surface normal shown in Fig. 9d is color coded such that red, green, and blue represent the x -, y -, and z -axis components, respectively.

Then, we evaluated the effectiveness of each constraint by determining the accuracy improvement of the surface normal when adding each constraint. Figure 10a–d show the surface normal results obtained from the SVD (Sect. 3.2), from the constant brightness constraint (Sect. 3.3), from the occluding boundary constraint (Sect. 4.2), and from the polarization angle refinement (Sect. 5.3), respectively. The reconstructed shape of Fig. 9d is shown in Fig. 11. Figure 12 and Table 2 show the error of the obtained surface normal compared to the true surface normal according to the constraints considered for estimation.

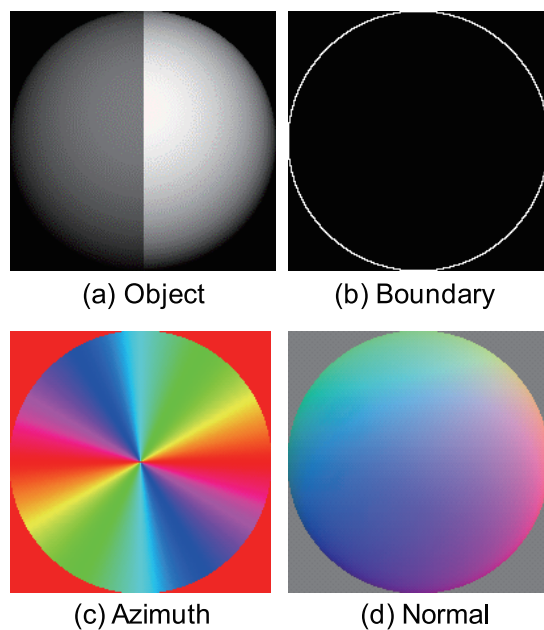


Fig. 9 Virtual sphere: **a** target object, **b** occluding boundary, **c** color-coded azimuth angle, and **d** color-coded surface normal

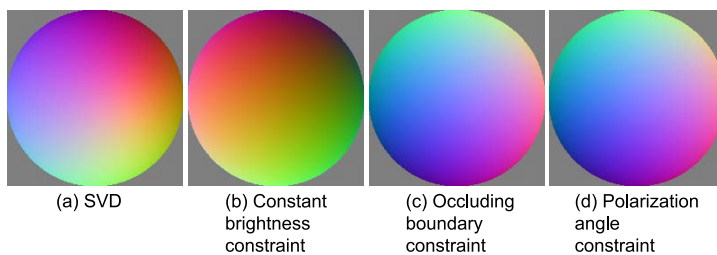


Fig. 10 Color-coded surface normal as the corresponding constraint is added to estimation

6.3 Result sphere

We captured 32 images of the real sphere shown in Fig. 13a to calculate its occluding boundary (Fig. 13b), azimuth angle (Fig. 13c), and surface normal (Fig. 13d).

Figure 14 and Table 3 show the error of the virtual and real spheres.

The surface normal results obtained when more constraints were integrated into the estimation are shown in Fig. 15, where the ground truth corresponds to the estimation result of calibrated photometric stereo with known light source directions. The reconstructed shape of the ground truth and that obtained using the proposed method are shown in Fig. 16a, b, respectively. The

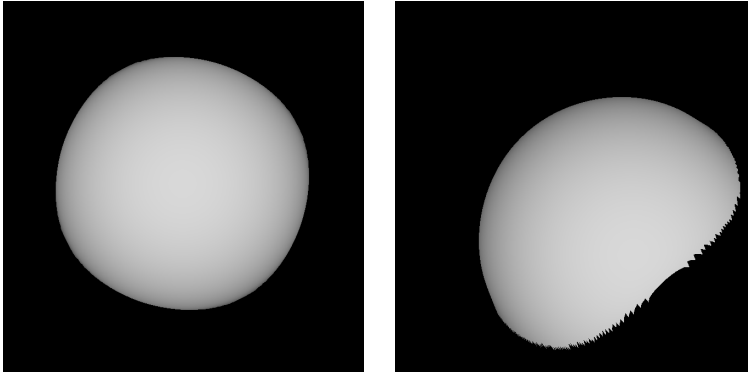


Fig. 11 Reconstructed shape of virtual sphere obtained from proposed method

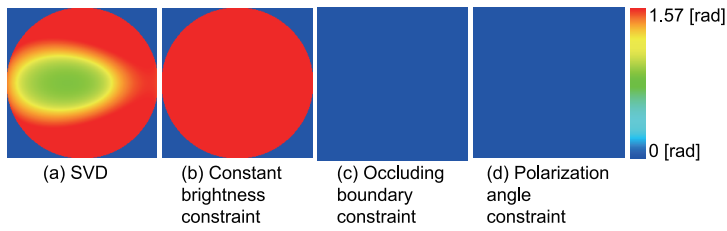


Fig. 12 Surface normal error of virtual sphere as corresponding constraint is added to estimation

Table 3 Surface normal error of virtual and real spheres

| | Virtual | Real |
|---------------------|---------|-------|
| Average error (rad) | 0.000 | 0.092 |
| Minimum error (rad) | 0.000 | 0.000 |
| Maximum error (rad) | 0.000 | 0.568 |

Table 4 Surface normal error of real sphere as corresponding constraint is added to estimation

| | SVD | Constant brightness | Occluding boundary | Polarization |
|---------------------|-------|---------------------|--------------------|--------------|
| Average error (rad) | 1.625 | 0.310 | 0.090 | 0.092 |
| Minimum error (rad) | 0.008 | 0.001 | 0.001 | 0.000 |
| Maximum error (rad) | 2.462 | 0.776 | 0.435 | 0.568 |

error between the proposed method and the theoretical value according to the constraints considered for estimation is detailed in Fig. 17 and Table 4. As discussed in the next section, the theoretical value represents the mathematical expression of the sphere.

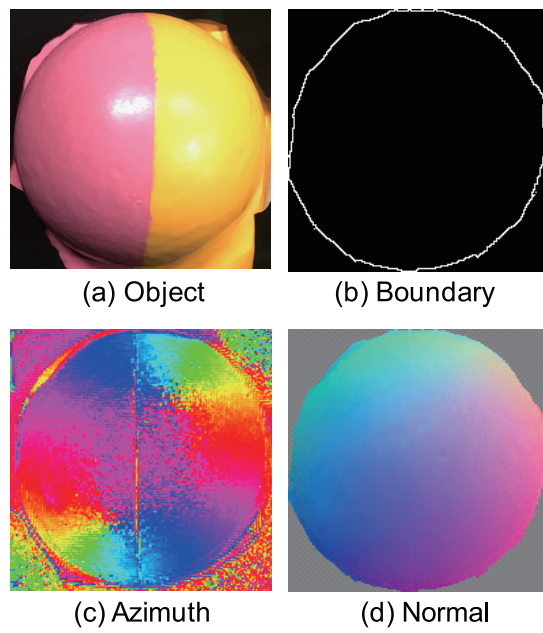


Fig. 13 Real sphere: **a** target object, **b** occluding boundary, **c** color-coded azimuth angle, and **d** color-coded surface normal

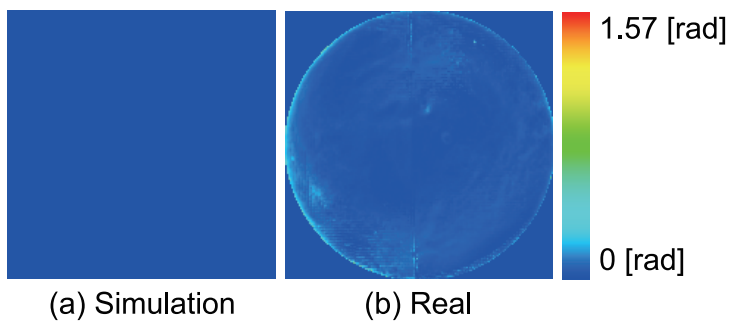


Fig. 14 Error of surface normal evaluation from virtual and real spheres

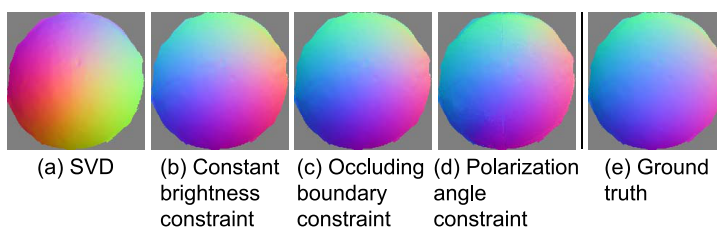


Fig. 15 Color-coded surface normal as corresponding constraint is added to estimation

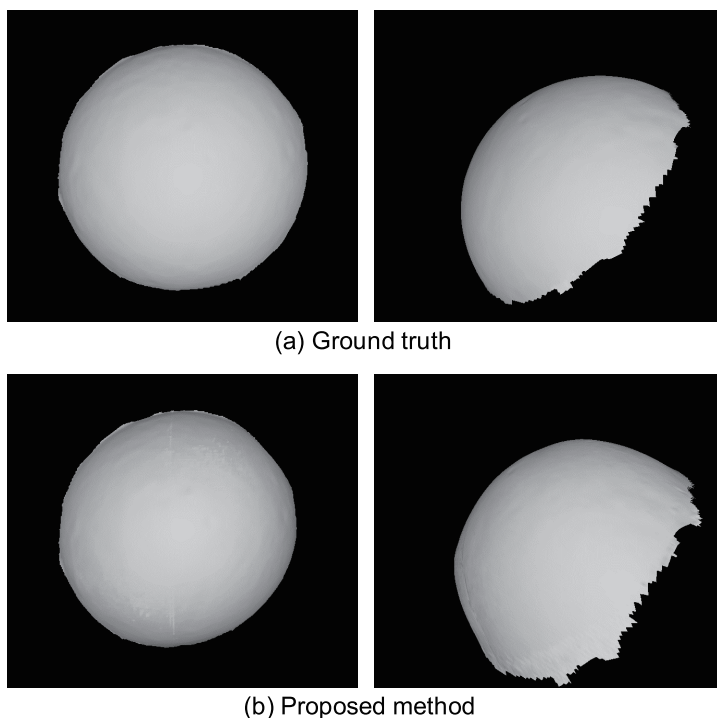


Fig. 16 Reconstructed shape of real sphere: **a** ground truth and **b** proposed method

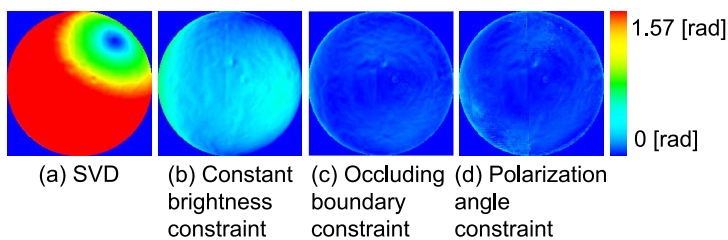


Fig. 17 Surface normal error of real sphere as corresponding constraint is added to estimation

6.4 Comparison of ground truth and theoretical value

Mathematically, the true surface normal can be obtained for a spherical shape; thus, using a sphere for evaluation is valid. However, the mathematically true surface normal is unknown for arbitrary objects; thus, the corresponding ground truths are required for evaluation. Here, we used the surface normal results obtained from calibrated photometric stereo with known light directions as ground truths. We evaluated a sphere to determine the suitability of

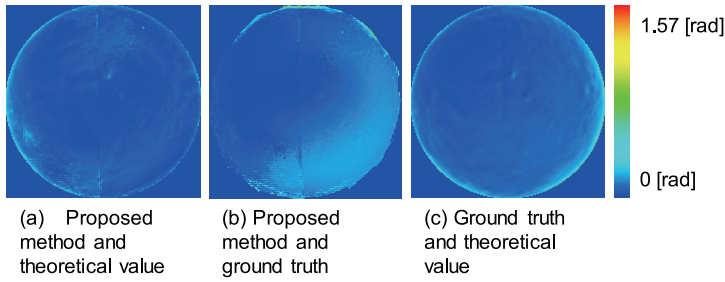


Fig. 18 Difference between surface normal results obtained from theoretical calculation, calibrated photometric stereo (ground truth), and proposed uncalibrated photometric stereo method

Table 5 Difference between results from theoretical calculation, calibrated photometric stereo (ground truth), and proposed uncalibrated photometric stereo method for plots shown in Fig. 18

| | (a) | (b) | (c) |
|---------------------|-------|-------|-------|
| Average error (rad) | 0.092 | 0.142 | 0.128 |
| Minimum error (rad) | 0.000 | 0.000 | 0.001 |
| Maximum error (rad) | 0.568 | 0.807 | 0.548 |

the surface normal obtained from calibrated photometric stereo as a ground truth, and the results are shown in Fig. 18 and Table 5.

The results confirm that calibrated photometric stereo can be used as ground truth; however, it does not provide the same results as the theoretical calculation. Therefore, evaluation using calibrated photometric stereo may not reflect the true value in some cases.

6.5 Common real objects

Figure 19a, b show a common object and its azimuth angle, respectively, and the surface normal results obtained from 29 input images are shown in Fig. 20. The ground truth obtained from the calibrated photometric stereo is shown in Fig. 21a, and the reconstruction obtained using the proposed method is shown in Fig. 21b. Figure 22 and Table 6 show the error of the obtained surface normal compared to the ground truth (obtained by calibrated photometric stereo) according to the constraints considered for estimation. The black part of the cat object is erroneous because we could not obtain information about the shape from either shading or polarization. In other words, it is impossible to obtain the shape of a black object by analyzing the diffuse reflection because no light is observed at the diffuse reflection of black objects.

Figures 23a, b show another object and its azimuth angle, respectively. In addition, the surface normal obtained from 32 input images according to the constraints considered for estimation is shown in Fig. 24. The ground truth

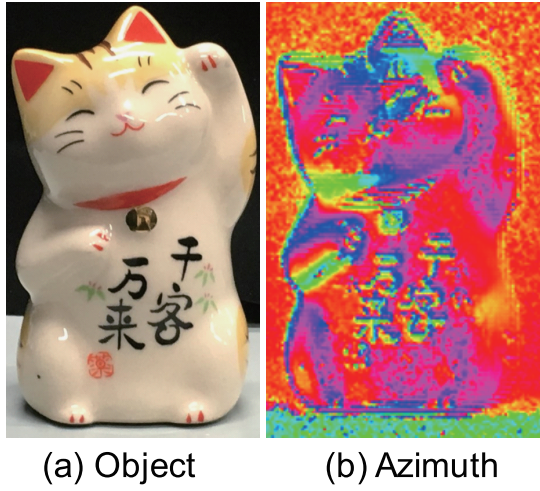


Fig. 19 Target object 1: **a** target object and **b** color-coded azimuth angle

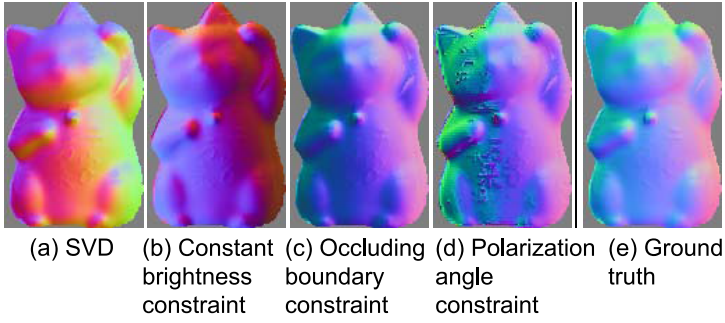


Fig. 20 Color-coded surface normal as corresponding constraint is added to estimation of object 1

Table 6 Surface normal error of object 1 as corresponding constraint is added in estimation

| | SVD | Constant brightness | Occluding boundary | Polarization |
|---------------------|-------|------------------------|-----------------------|--------------|
| Average error (rad) | 1.545 | 1.435 | 0.633 | 0.564 |
| Minimum error (rad) | 0.038 | 0.017 | 0.022 | 0.013 |
| Maximum error (rad) | 2.551 | 2.375 | 0.951 | 2.293 |

obtained from calibrated photometric stereo is shown in Fig. 25a, and the shape reconstructed by the proposed method is shown in Fig. 25b. Figure 26 and Table 7 show the error of the obtained surface normal according to the constraints considered for estimation.

Figure 27a, b show a third object and its azimuth, respectively. The surface normal obtained from 30 input images according to the constraints considered

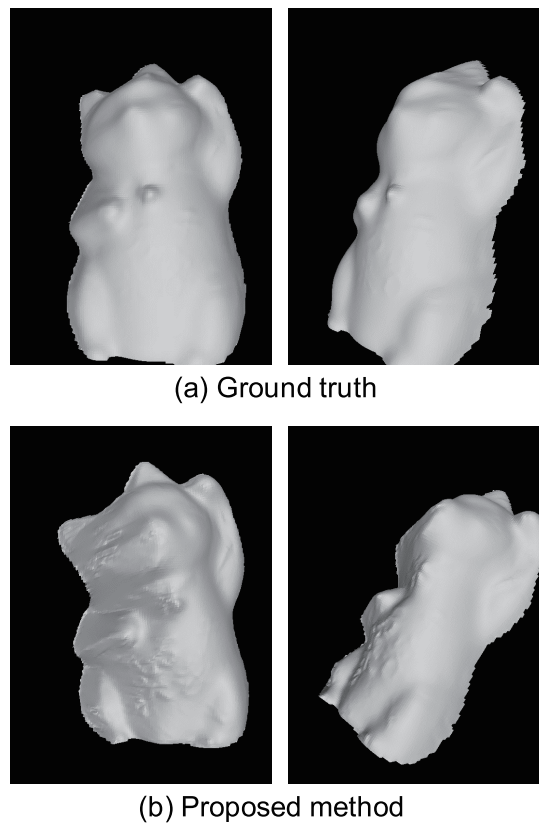


Fig. 21 Reconstructed shape of object 1: **a** ground truth and **b** proposed method

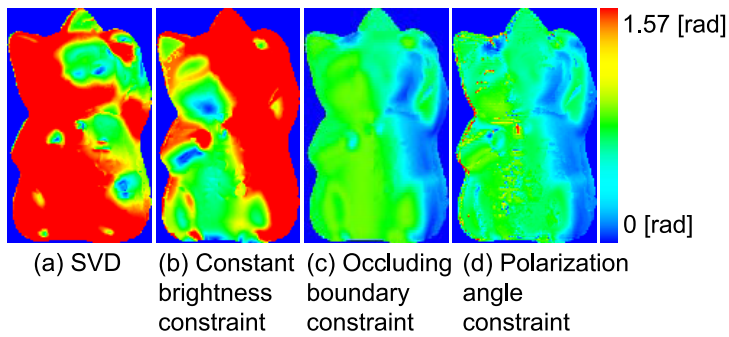


Fig. 22 Performance comparison for each constraint

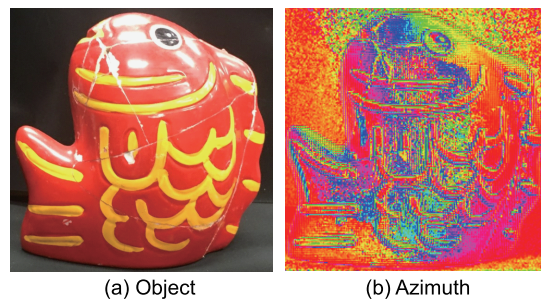


Fig. 23 Target object 2: **a** target object and **b** color-coded azimuth angle

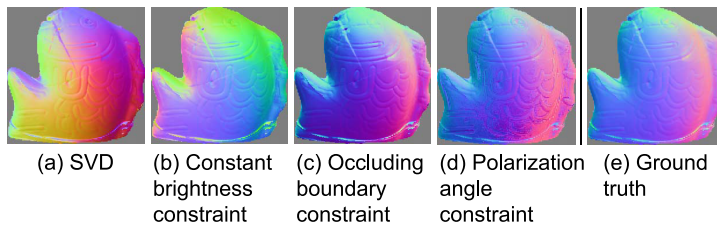


Fig. 24 Color-coded surface normal as corresponding constraint is added to estimation of object 2

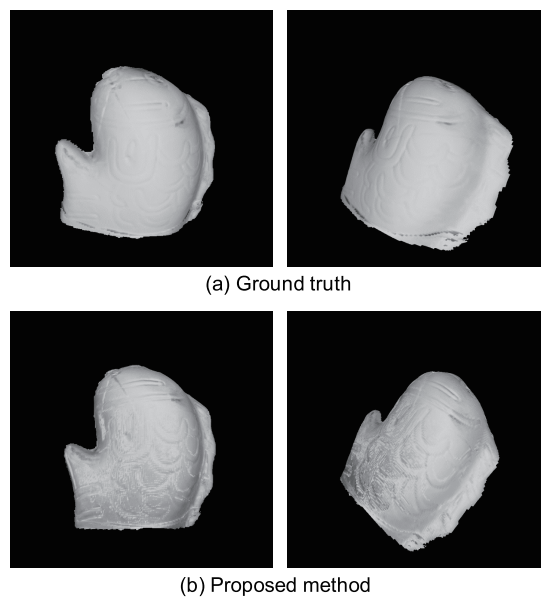


Fig. 25 Reconstructed shape of object 2: **a** ground truth and **b** proposed method

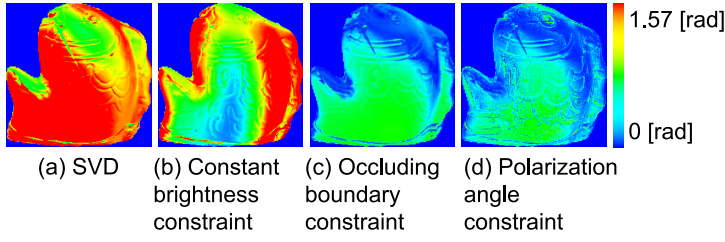


Fig. 26 Surface normal of object 2 as corresponding constraint is added to estimation

Table 7 Surface normal error of object 2 as corresponding constraint is added to estimation

| | SVD | Constant brightness constraint | Occluding boundary constraint | Polarization |
|---------------------|-------|--------------------------------------|-------------------------------------|--------------|
| Average error (rad) | 1.629 | 1.103 | 0.445 | 0.359 |
| Minimum error (rad) | 0.682 | 0.198 | 0.005 | 0.002 |
| Maximum error (rad) | 3.126 | 2.680 | 0.811 | 1.413 |

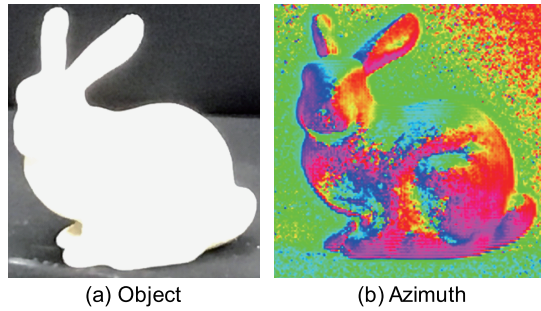


Fig. 27 Target object 3: **a** target object and **b** color-coded azimuth angle

Table 8 Surface normal error of object 3 as corresponding constraint is added to estimation

| | SVD | Constant brightness constraint | Occluding boundary constraint | Polarization |
|---------------------|-------|--------------------------------------|-------------------------------------|--------------|
| Average error (rad) | 1.317 | 1.023 | 0.955 | 0.862 |
| Minimum error (rad) | 0.005 | 0.014 | 0.299 | 0.028 |
| Maximum error (rad) | 2.467 | 2.054 | 1.485 | 3.028 |

for estimation is shown in Fig. 28. The ground truth obtained from calibrated photometric stereo is shown in Fig. 29a, and the reconstructed shape obtained using the proposed method is shown in Fig. 29b. Figure 30 and Table 8 show the error of the obtained surface normal according to the constraints considered for estimation. As can be seen, the neck and breast of the rabbit are not well reconstructed due to interreflection. Handling interreflection is quite difficult because polarization is depolarized during interreflection.

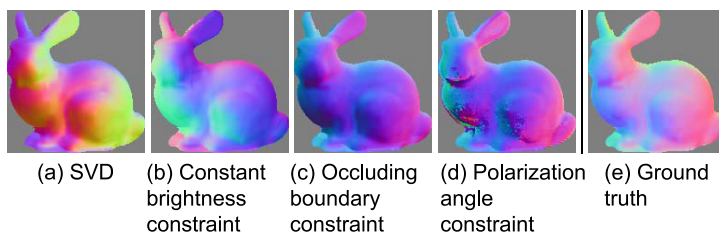


Fig. 28 Color-coded surface normal as corresponding constraint is added to estimation of object 3

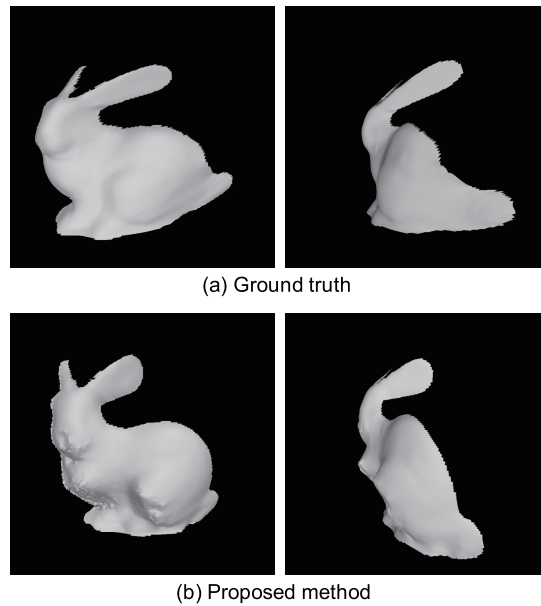


Fig. 29 Reconstructed shape of object 3: **a** ground truth and **b** proposed method

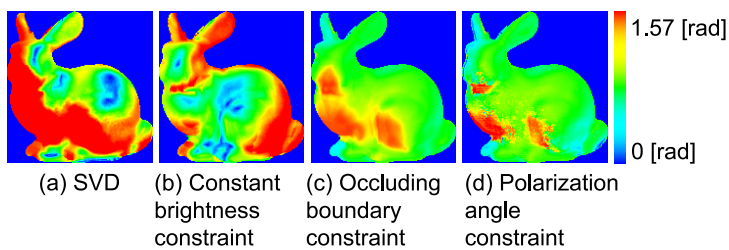


Fig. 30 Surface normal error of object 3 as corresponding constraint is added to estimation

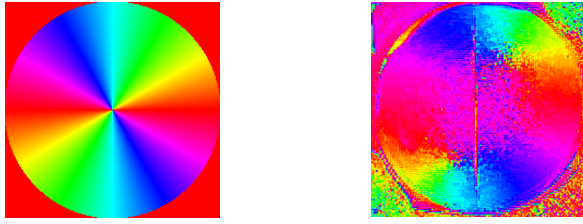


Fig. 31 True azimuth angle (left) and azimuth angle (right) obtained from a sphere under pollution by faint surrounding light

7 Discussion

The results demonstrate the effectiveness of the constraints used in the proposed method. The occluding boundary provides a strong cue for uncalibrated photometric stereo. In addition, the calculation of the surface normal is not affected by the albedo difference, and the surface normal at a pixel with specular reflection is also obtained correctly, which indicates the contribution of linearization in photometric stereo.-

However, some limitations of the proposed method should be addressed. The proposed method, like other photometric stereo methods, cannot be applied to black objects. In addition, the accuracy of the obtained azimuth angle may be low because polarization can be easily polluted by even faint surrounding light, as shown in Fig. 31. As can be seen in Fig. 7, the degree of polarization is low for diffuse reflection and thus sensitive to noise. Finally, the azimuth angle can only constrain the x - and y -axis components of the surface normal, whereas the z -axis component is not improved by polarization.

A potential solution to these limitations may be to use the degree of polarization of specular reflection. Even if the diffuse reflection is black, a smooth object causes specular reflection. As the degree of polarization of specular reflection is higher than that of diffuse reflection, the azimuth angle is more reliable. In addition, the degree of polarization gives a cue for the z -axis component of the surface normal. In addition, there is a problem relative to the degree of polarization, i.e., the surface roughness parameter and IOR should be known (Fig. 7). Moreover, this solution does not work for objects without specular reflection. Thus, future plans to improve the proposed method should be considered carefully.

8 Conclusion

In this paper, we have verified that polarization provides a strong cue to enhance uncalibrated photometric stereo. In the proposed method, we use multiple polarization images with illumination from by faint surrounding light different directions from a single light source as input data. Then, photometric linearization is employed to remove specular reflection. We solve the ambiguity

of uncalibrated photometric stereo by assuming the light brightness to be constant and that the surface normal at the occluding boundary points is directed orthogonally outward. The azimuth angle calculated from the polarization data refines the surface normal calculated using uncalibrated photometric stereo. The experimental results demonstrated the high performance of the proposed method when estimating the surface normal of an object.

In future, we plan to prepare an experimental environment to obtain polarization data accurately. We also plan to implement a constraint to improve the estimation of the z -axis component of the surface normal. Although the polarization degree contains such information, it depends on the refractive index and roughness of surface. Thus, we also plan to explore other information sources besides the polarization degree to obtain the z -axis component of the surface normal.

Compliance with ethical standards

Conflict of interest The authors declare that they have no competing interests.

References

1. Woodham, R. J.: Photometric method for determining surface orientation from multiple images. *Opt. Eng.* **19**(1), 191139 (1980). <https://doi.org/10.1117/12.7972479>
2. Woodham, R.J., Iwahori, Y., Barman, R.A.: Photometric stereo: Lambertian reflectance and light sources with unknown direction and strength. In: Technical Reports, The University of British Columbia, TR-91-18, 11 pp. (1991)
3. Hayakawa, H.: Photometric stereo under a light source with arbitrary motion. *J. Opt. Soc. Am. A* **11**(11), 3079–3089 (1994). <https://doi.org/10.1364/JOSAA.11.003079>
4. Yuille, A.L., Snow, D., Epstein, R., Belhumeur, P.N.: Determining generative models of objects under varying illumination: Shape and albedo from multiple images using SVD and integrability. *Int. J. Comput. Vis.* **35**(3), 203–222 (1999). <https://doi.org/10.1023/A:1008180726317>
5. Alldrin, N.G., Mallick, S.P., Kriegman, D.J.: Resolving the generalized bas-relief ambiguity by entropy minimization. In: Proceedings of IEEE Conference on Computer Vision and Pattern Recognition, pp. 1–7 (2007). <https://doi.org/10.1109/CVPR.2007.383208>
6. Belhumeur, P.N., Kriegman, D.J., Yuille, A.L.: The bas-relief ambiguity. *Int. J. Comput. Vis.* **35**, 33–44 (1999). <https://doi.org/10.1023/A:1008154927611>
7. Shi, B., Matsushita, Y., Wei, Y., Xu, C., Tan, P.: Self-calibrating photometric stereo. In: Proceedings of IEEE Computer Society Conference on Computer Vision and Pattern Recognition, pp. 1118–1125 (2010). <https://doi.org/10.1109/CVPR.2010.5540091>
8. Basri, R., Jacobs, D., Kemelmacher, I.: Photometric stereo with general, unknown lighting. *Int. J. Comput. Vis.* **72**(3), 239–257 (2007). <https://doi.org/10.1007/s11263-006-8815-7>
9. Sato, I., Okabe, T., Yu, Q., Sato, Y.: Shape reconstruction based on similarity in radiance changes under varying illumination. In: Proceedings of International Conference on Computer Vision, pp. 1–8 (2007). [<https://doi.org/10.1109/ICCV.2007.4409020>]
10. Drbohlav, O., Šára, R.: Specularities reduce ambiguity of uncalibrated photometric stereo. In: A. Heyden, G. Sparr, M. Nielsen, P. Johansen (eds.) *Computer Vision -ECCV 2002*, Lecture Notes in Computer Science, vol. 2351. Springer, Berlin, Heidelberg (2002). [https://doi.org/10.1007/3-540-47967-8_4]

11. Georghiades, A.S.: Incorporating the Torrance and Sparrow model of reflectance in uncalibrated photometric stereo. In: Proceedings of IEEE International Conference on Computer Vision, vol. 2, pp. 816–825 (2003). <https://doi.org/10.1109/ICCV.2003.1238432>
12. Chandraker, M.K., Kahl, F., Kriegman, D.J.: Reflections on the generalized bas-relief ambiguity. In: Proceedings of IEEE Computer Society Conference on Computer Vision and Pattern Recognition, vol. 1, pp. 788–795 (2005). <https://doi.org/10.1109/CVPR.2005.299>
13. Mo, Z., Shi, B., Lu, F., Yeung, S., Matsushita, Y.: Uncalibrated photometric stereo under natural illumination. In: IEEE/CVF Conference on Computer Vision and Pattern Recognition, pp. 2936–2945 (2018). <https://doi.org/10.1109/CVPR.2018.00310>
14. Favaro, P., Papadimitriou, T.: A closed-form solution to uncalibrated photometric stereo via diffuse maxima. In: Proceedings of IEEE Conference on Computer Vision and Pattern Recognition, pp. 821–828 (2012). <https://doi.org/10.1109/CVPR.2012.6247754>
15. Wu, Z., Tan, P.: Calibrating photometric stereo by holistic reflectance symmetry analysis. In: Proceedings of IEEE Conference on Computer Vision and Pattern Recognition, pp. 1498–1505 (2013). <https://doi.org/10.1109/CVPR.2013.197>
16. Wolff, L.B., Boult, T.E.: Constraining object features using a polarization reflectance model. *IEEE Transact. Pattern Anal. Mach. Intell.* **13**(7), 635–657 (1991). <https://doi.org/10.1109/34.85655>
17. Rahmann, S., Canterakis, N.: Reconstruction of specular surfaces using polarization imaging. In: Proceedings of IEEE Computer Society Conference on Computer Vision and Pattern Recognition, pp. I–I (2001). <https://doi.org/10.1109/CVPR.2001.990468>
18. Atkinson, G.A., Hancock, E.R.: Shape estimation using polarization and shading from two views. *IEEE Transact. Pattern Anal. Mach. Intell.* **29**(11), 2001–2017 (2007). <https://doi.org/10.1109/TPAMI.2007.1099>
19. Atkinson, G.A., Hancock, E.R.: Recovery of surface orientation from diffuse polarization. *IEEE Transact. Image Process.* **15**(6), 1653–1664 (2006). <https://doi.org/10.1109/TIP.2006.871114>
20. Huynh, C.P., Robles-Kelly, A., Hancock, E.R.: Shape and refractive index from single-view spectro-polarimetric images. *Int. J. Comput. Vis.* **101**, 64–94 (2013). <https://doi.org/10.1007/s11263-012-0546-3>
21. Atkinson, G.A., Hancock, E.R.: Surface reconstruction using polarization and photometric stereo. In: W. G. Kropatsch, M. Kampel, A. Hanbury (eds.) *Computer Analysis of Images and Patterns, CAIP 2007, Lecture Notes in Computer Science*, vol. 4673. Springer, Berlin, Heidelberg (2007). https://doi.org/10.1007/978-3-540-74272-2_58
22. Drbohlav, O., Sara, R.: Unambiguous determination of shape from photometric stereo with unknown light sources. In: Proceedings of IEEE International Conference on Computer Vision, vol. 1, pp. 581–586 (2001). <https://doi.org/10.1109/ICCV.2001.937570>
23. Ngo, T.T., Nagahara, H., Taniguchi, R.: Shape and light directions from shading and polarization. In: IEEE Conference on Computer Vision and Pattern Recognition, pp. 2310–2318 (2015). <https://doi.org/10.1109/CVPR.2015.7298844>
24. Mukaigawa, Y., Ishii, Y., Shakunaga, T.: Analysis of photometric factors based on photometric linearization. *J. Opt. Soc. Am. A* **24**(10), 3326–3334 (2007). <https://doi.org/10.1364/JOSAA.24.003326>
25. Tomasi, C., Kanade, T.: Shape and motion from image streams under orthography: A factorization method. *Int. J. Comput. Vis.* **9**, 137–154 (1992). <https://doi.org/10.1007/BF00129684>
26. Shum, H., Ikeuchi, K., Reddy, R.: Principal component analysis with missing data and its application to polyhedral object modeling. *IEEE Transact. Pattern Anal. Mach. Intell.* **17**(9), 854–867 (1995). <https://doi.org/10.1109/34.406651>
27. Wu, L., Ganesh, A., Shi, B., Matsushita, Y., Wang, Y., Ma, Y.: Robust photometric stereo via low-rank matrix completion and recovery. In: R. Kimmel, R. Klette, A. Sugimoto (eds.) *Computer Vision - ACCV 2010, Lecture Notes in Computer Science*, vol. 6494. Springer, Berlin, Heidelberg (2010). https://doi.org/10.1007/978-3-642-19318-7_55
28. Ikehata, S., Wipf, D., Matsushita, Y., Aizawa, K.: Photometric stereo using sparse Bayesian regression for general diffuse surfaces. *IEEE Transact. Pattern Anal. Mach. Intell.* **39**(9), 1816–1831 (2014). <https://doi.org/10.1109/TPAMI.2014.2299798>

29. Mori, T., Taketa, R., Hiura, S., Sato, K.: Photometric linearization by robust PCA for shadow and specular removal. In: G. Csurka, M. Kraus, R. S. Laramée, P. Richard, J. Braz (eds.) *Computer Vision, Imaging and Computer Graphics, Theory and Application*, Communications in Computer and Information Science, vol. 359. Springer, Berlin, Heidelberg (2013). https://doi.org/10.1007/978-3-642-38241-3_14
30. Miyazaki, D., Ikeuchi, K.: Photometric stereo under unknown light sources using robust SVD with missing data. In: *Proceedings of IEEE International Conference on Image Processing*, pp. 4057–4060 (2010). <https://doi.org/10.1109/ICIP.2010.5650067>
31. Wolff, L.B., Lundberg, A., Tang, R.: Image understanding from thermal emission polarization. In: *Proceedings of IEEE Computer Society Conference on Computer Vision and Pattern Recognition*, pp. 625–631 (1998). <https://doi.org/10.1109/CVPR.1998.698670>